Triangular Curvature Approximation of Surfaces
Filtering the Spurious Mode

Paavo Nevalainen[1], Ivan Jambor[2], Jonne Pohjankukka[1], Jukka Heikkonen[1] and Tapio Pahikkala[1]
[1]*Dept. of Information Tech., Univ. of Turku, FI-20014 Turku, Finland*
[2]*Dept. of Diagnostic Radiology, Univ. of Turku, FI-20014 Turku, Finland*
{*ptneva, ivjamb, jonne.pohjankukka, jukhei,tapio.pahikkala*}*@utu.fi*

Keywords: Curvature Spectrum, Parameterless Filtering, Irregular Triangulated Networks, Discrete Geometry.

Abstract: Curvature spectrum is a useful feature in surface classification but is difficult to apply to cases with high noise typical e.g. to natural resource point clouds. We propose two methods to estimate the mean and the Gaussian curvature with filtering properties specific to triangulated surfaces. Methods completely filter a highest shape mode away but leave single vertical pikes only partially dampened. Also an elaborate computation of nodal dual areas used by the Laplace-Beltrami mean curvature can be avoided. All computation is based on triangular setting, and a weighted summation procedure using projected tip angles sums up the vertex values. A simplified principal curvature direction definition is given to avoid computation of the full second fundamental form. Qualitative evaluation is based on numerical experiments over two synthetical examples and a prostata tumor example. Results indicate the proposed methods are more robust to presence of noise than other four reference formulations.

1 INTRODUCTION

Wide-scale point clouds have become accessible to analysis everywhere. The point cloud surface registration typically has an approximate or accurate Delaunay triangular or tetrahedral mesh generation as a preliminary step. The surface models are called irregular triangularized networks (TIN) for historical reasons. The application domains can be roughly divided to three categories by the target environment: built environment, natural resource data and medical 3D imaging.

The ratio $0 \leq \sigma_h/r \leq 0.3$ of the perpendicular noise component σ_h and the nominal surface radius r describe the difficulty of curvature registration. The built environment data has usually high point density and small noise ratio compared to the natural resource data (Mitra and Nguyen, 2003). Built surfaces are usually solid, curvature values change slowly over distance, and it is desirable to be able to detect the local curvature accurately. A typical mean curvature method for such data is based on the Laplace-Beltrami (L-B) operator (Meyer et al., 2003; Mesmoudi et al., 2012).

Other two application domains have the noise ratio much higher, approximately $\sigma_h/r = 10^{-2}...10^{-1}$ (Schaer et al., 2007). Surfaces, e.g. the terrain surface, are porous, covered with vegetation or mathematically undefined. Natural resource data is gatherer by aerial light detection and ranging (LiDAR) or by spatial photogrammetry. Natural resource data has shape recognition tasks where the point samples per target ratio reaches one (Nevalainen et al., 2016), i.e. one single elevated hit is a possible target (e.g. a surface stone), see Fig. 1. Detection of an individual target is naturally uncertain in the presence of noise, but one can cluster larger areas e.g. to stony or non-stony ones using e.g. the curvature spectrum (Nevalainen et al., 2015). On the other hand, there is a natural frequency limit defined by the nominal mesh length. Excitation of this frequency over a large area (see Fig. 1 left side) is

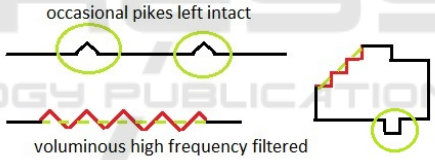

Figure 1: The voluminous highest noise component arises either from the scanning process (LiDAR point clouds, left), or from the voxel granularity (right). Neither case should require any parameters to filter. Occasional anomalies (circles) should be transferred intact to pattern recognition phase.

Nevalainen, P., Jambor, I., Pohjankukka, J., Heikkonen, J. and Pahikkala, T.
Triangular Curvature Approximation of Surfaces - Filtering the Spurious Mode.
DOI: 10.5220/0006249206840692
In *Proceedings of the 6th International Conference on Pattern Recognition Applications and Methods (ICPRAM 2017)*, pages 684-692
ISBN: 978-989-758-222-6

usually a numerical artifact which should be filtered at some point of the processing.

Medical 3D applications, especially magnetic resonance imaging (MRI), often have non-isotropic voxels causing excitation at the frequency limit, see right part of the Fig. 1. Numerical methods should be resilient to effect of noise, low sampling and discretization patterns.

Surface registration is reminiscent of interpolation, whereas noise reduction is filtering. Typically, these two operations can be performed in any order, or combined together. Spatial filtering requires several parameters, and it is worthwhile to seek curvature registration methods, which would handle the highest frequency as depicted in Fig. 1:

1. leaving single pikes to be handled by later pattern recognition and filtering steps.
2. eliminating automatically large excitations of the highest frequency.

Naturally, if such a behaviour is squarely against the needs of a specific application, there is an abundant supply of existing curvature registration methods, which should be employed instead. Alternative methods have several opposing properties for discrete differential operators (Wardetzky et al., 2007) used as building blocks for curvature analysis. If a new application field arises, one has to be aware of the tradeoffs between different properties.

The Gaussian and mean curvature completely define the local curvature of any continuous surface. It is the consensus of the current research that the local Gaussian curvature is best estimated on TIN models by so called angle deficit (see e.g. (Crane et al., 2013), and the result is robust to noise. This reference method is named as vertex Gaussian in this paper.

This paper uses the classical differential geometric definition of the average Gaussian curvature (Pressley, 2010): it is the ratio of the total orientation change over a surface area, a TIN triangle in this case. It is pointed out in Sec. 3.1 that this simple definition leads to a triangular Gaussian curvature estimation on vertices, which fills the requirements 1 and 2 mentioned before.

The mean curvature is numerically more difficult target than Gaussian curvature. One starting point for computation has been neglected in the literature thus far. It is possible to define the mean curvature by the local rate of change of the surface area when the surface is mapped towards the direction of its unit normal (Pressley, 2010). This definition is related to the theory of minimal surfaces and it can be applied directly to the triangulated surface with defined vertex normals. Also this novel mean curvature formulation has the earlier mentioned properties 1 and 2, as ruminated in Sec. 3.1.

The rest of the paper has the following structure: Section 2 introduces the triangular Gaussian and mean curvatures, and a collection of competing definitions. Also the problem of finding the principal curvature direction has been addressed there. Section 3 has a practical example (prostata tumor), and two synthetical test cases to verify the properties 1 and 2 of the proposed method. Section 4 brings in the conclusions.

2 TRIANGULAR CURVATURE

The following notation will be used throughout the presentation. The set of cloud points $\mathcal{P} \subset \mathbb{R}^3$ is given. A triangle $t = (a,b,c), a,b,c \in \mathcal{T} \subset \mathcal{P}^3$ is defined by three vertex points which can be referred in cyclic fashion in counterclockwise order (with three possible combinations considered identical). To shorten the notation, the vertex membership $a \in t$ and the geometric insidence $q \in t$ have the same notation, when the intended meaning is clear from the context. A vertex p has a set of surrounding triangles $T_p = \{t \in \mathcal{T} | p \in t\} \subset \mathcal{T}$. The edge neighborhood $N_p = \cup_{t \in T_p} t \setminus \{p\}$ is a counterclockwise cyclically ordered set of points connected to p by a triangle edge.

The triangle $t = \{a,b,c\}$ has a unique face normal n_t (oriented outwards) and an area A_t:

$$N_t = (b-a) \times (c-a)$$
$$A_t = \|N_t\|/2 \quad (1)$$
$$n_t = N_t^0, \quad (2)$$

where N_t is a temporary cross product term and vector power $v^0 = v/\|v\|$ of a vector v denotes the vector normalization.

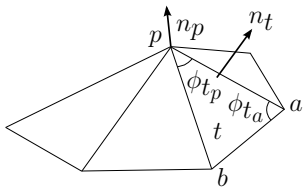

Figure 2: Triangle concepts: tip angles ϕ_{tp} are indexed by vertices p of triangles t. Also the vertex normal n_p and face normal n_t depicted.

The local curvature state of the surface is completely defined after finding out both mean curvature H and the Gaussian curvature G. Sections 2.1- 2.7 present the curvature quantities both in a triangle t and at a vertex p.

2.1 Triangular Gaussian Curvature

The tangential orientation change $\Delta\alpha$ over a length l defines κ, the average of the curvature of a 2D curve over the same length: $\kappa = \Delta\alpha/l$. Analogous to this, the average of the Gaussian curvature of a smooth surface $S \subset \mathbb{R}^3$ can be defined (Pressley, 2010, p.166-168) as the ratio $G_S = \omega_S/A_S$, where A_S is the surface area of S and ω_S is the solid angle of which the surface normal $n(q), q \in S$ traces. This definition can be applied to a triangle $t = \{a,b,c\}$ with vertex normals n_a, n_b, n_c with the exception that the accurate surface S is not known and the triangle area A_t is a lower bound approximation of the hypothetical smooth area $meas(S_q)$. Ramifications of this fact will be addressed in Sec. 3.1.

The solid angle ω_t in Eq. 3 is the total trace of normal $n(q)$, $q \in t$ and, assuming a barycentric interpolation scheme, it equals the solid angle of a vector tri-blade n_a, n_b, n_c (van Oosterom and Strackee, 1983):

$$\tan(\omega_t/2) = \frac{n_a \cdot n_b \times n_c}{1 + n_a \cdot n_b + n_b \cdot n_c + n_c \cdot n_a} \quad (3)$$

$$G_t = \omega_t / A_t. \quad (4)$$

The numerator in Eq. 3 equals zero when at least two vertex normals are parallel, which results in requirements 1 and 2 of Sec. 1 to be fulfilled as far as triangular Gaussian G_t of Eq. 4 is concerned. This will be elaborated further in Sec. 3.1.

2.2 Triangular Mean Curvature

Considering a triangle $t = (a,b,c)$ and the associated surface normal approximants n_a, n_b, n_c at vertices a,b,c, and a barycentric dependency of normals $n(q), q \in t$ in the triangle t, one can define a normal mapped parallel triangle $t^u = \{q + u\,n(q) \,|\, q \in t\}$. Using a definition of (an averaged) mean curvature in (Pressley, 2010, p. 207), one gets:

$$H_t = \frac{1}{2A_t}\left(\frac{d}{du} A_{t^u}|_{u=0}\right) = \frac{(n_b - n_a) \times (c-a) + (b-a) \times (n_c - n_a)}{4A_t} \cdot n_t. \quad (5)$$

Note that triangular mean curvature $H_t \equiv 0$ when all the vertex unit normals are parallel i.e. $n_a = n_b = n_c$. This leads to requirements 1 and 2 of Sec. 1 to be fulfilled.

2.3 Projective Tip Angles as Weights

The vector angle function acos() and the projected vector angle function $\text{acos}_n()$ simplify the upcoming presentation. The projection angle ϕ'_{12} is the angle ϕ'_{12} between vectors v_1 and v_2 when seen from direction n. See the right part of the Fig. 3. A projection matrix $P(n) = I - n^0 n^{0T}$ is used to define $\text{acos}_n(.)$:

$$\text{acos}(v_1, v_2) = \cos^{-1}(v_1^0 \cdot v_2^0) \quad (6)$$

$$v'_i = P(n) v_i,\ i = 1,2$$

$$\text{acos}_n(v_1, v_2) = \text{acos}(v'_1, v'_2). \quad (7)$$

Note that $\text{acos}(v_1, v_2) \equiv \text{acos}_{v_1 \times v_2}(v_1, v_2)$.

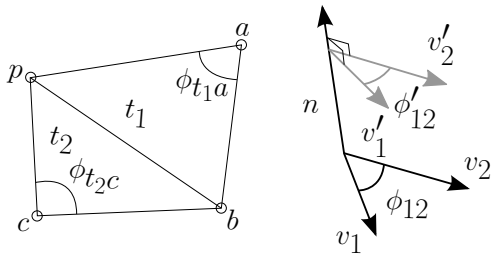

Figure 3: Left: the angle ϕ_{12} between two vectors v_1, v_2 and the projected angle ϕ'_{12} between projected vectors v'_1, v'_2. Right: Definition of the edge angles $\phi_{t'tq}$ and $\phi_{t'q'}$ of an edge (p,q).

The projective tip angles ϕ'_{tp} are used systematically to average all triangular quantities $X_t, t \in \mathcal{T}$ to corresponding vertex quantities X_p, $p \in \mathcal{P}$:

$$\phi'_{t_1 a} = \text{acos}_{n_p}(p-a, b-a) \text{ (See Fig. 3)} \quad (8)$$

$$\phi'_p = \sum_{t \in T_p} \phi'_{tp} \quad (9)$$

$$X_p = \sum_{t \in T_p} \phi'_{tp} X_t / \phi'_p. \quad (10)$$

This weighting procedure of a quantity X will be denoted as: $X_t \to X_p$ in the rest of the text.

Good numerical properties of tip angle weighting pointed us to amortize the computational costs by applying it to produce the following vertex properties: normals n_p, triangular mean curvature H_p, triangular Gaussian G_p and principal curvature direction v_p. Another benefit was the unified handling of the boundary points, since the angle sums $\phi'_p \leq \phi_p \leq 2\pi$ give an excellent weighting at the boundary. This is important because e.g. the natural resource data is prune to have missing values and holes in the point cloud, and the boundary points are thus common. When a point p is not in the border, the sum of projected angles equals: $\phi'_p \equiv 2\pi$. There are other weighting schemes in the literature, these are being discussed in Sections 2.5 and 2.6.

2.4 Vertex Gaussian

Since the projected tip angles have been introduced, it is possible to define an alternative vertex Gaussian using the spherical excess (Crane et al., 2013) formulation. The vertex Gaussian of Eq. 12 serves as a re-

ference method:

$$\phi_p = \sum_{t\in T_p} \phi_{tp} \quad (11)$$

$$G_p = (\phi'_p - \phi_p)/(A_p/3). \quad (12)$$

2.5 Vertex Normals

Vertex normals n_p are weighted from triangle normals n_t using the generic scheme of projected tip weighting defined in Eq. 10: $n_t \rightarrow n_p$. There are several other possible definitions. Vertex normals can be considered pointing towards the new altered vertices after the local surface is varied, or they somehow represent a continuous but unknown reference positions. The alternatives satisfying DDG convergence requirements listed in (Crane et al., 2013) are reproduced here for discussion. The vertex normal can be:

1. The vector area: $n_p = \left(\sum_{t\in T_p} A_t n_t\right)^0$
2. The area (or volume) gradient $n_p = (dA_p/dp)^0$, when one vertex p is varied in $\mathbb{R}^3$.
3. The normal of a sphere which inscribes vertex p and its edge-neighborhood points N_p. See (Max, 1999; Crane et al., 2013).

Such a sphere fitting required by the alternative 3 is impossible with usual point clouds, but just applying the definition from a case of a perfect sphere fit to any general triangle neighborhood, the resulting normal vector n_p behaves smoothly:

$$n_p = \left(\sum_{t=(a,p,b)\in T_p} \frac{n_t}{\|b-p\|\|a-p\|}\right)^0.$$

According to (Jin et al., 2005), versions 1 and 2 are simple but prune to noise, projected tip angle weighting (our choice) is reliable and simple, and version 3 is rather good but also somewhat expensive.

2.6 Other Mean Curvature Definitions

This short survey omits all methods based on a local fit of a smooth interpolant, see e.g. (Yang and Qian, 2007). These methods show resilience to noise, but tend to have an uncontrollable loss of high frequencies and are usually computationally more expensive than the methods presented in the following.

The mean curvature through the discrete Laplace-Beltrami (also known as the cotan-Laplace) operator has been documented in (Mesmoudi et al., 2012). It is one of the best methods according to (Mesmoudi et al., 2012). The mean curvature H_p at a vertex p becomes:

$$H_p = \frac{1}{4A'_p}\left\|\sum_{b\in N_p}\left(\frac{1}{\tan\phi_{t_1 a}} + \frac{1}{\tan\phi_{t_2 c}}\right)(b-p)\right\|, \quad (13)$$

where triangles $t_1, t_2 \in T_p$ have a common edge (p,b) with opposite vertex angles $\phi_{t_1 a}, \phi_{t_2 b}$. See Fig. 3. The vertex specific area $A'_p \approx A_P/3$ is the area of so called mixed Voronoi cell. Using A'_p instead of $A_p/3$ reduces the area contribution of possible obstuse angles ϕ_{tp} in a way, which is detailed in (Mesmoudi et al., 2012). The exact value of A'_p depends on the geometry of the triangle set T_p but is always rather close to the above given expected average. The variance in A'_p adds numerical stability of the estimates of the vertex mean curvature H_p but is rather costly to calculate.

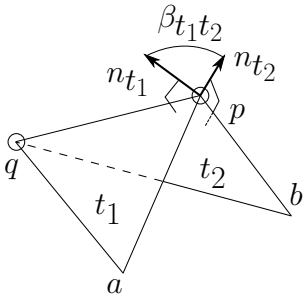

Figure 4: The edge angle $\beta_{t_1 t_2}$ is positive when the edge folds downwards (or inwards in case of tumors).

The concentrated Gaussian curvature by (Mesmoudi et al., 2012) equals Eq. 12. The concentrated mean curvature by (Mesmoudi et al., 2012) is re-cast to the notation in this paper as:

$$sgn(t_1,t_2) = -sgn((b-p)\cdot n_{t_1}) \quad (14)$$

$$\beta_{t_1t_2} = \text{acos}(n_{t_1}, n_{t_2}) sgn(t_1,t_2) \quad (15)$$

$$\omega_p = 2\pi - \sum_{t_1\in T_p} \beta_{t_1t_2} \quad (16)$$

$$H_p = \frac{1}{4A'_p}(2\pi - \omega_p), \quad (17)$$

where the edge angles $\beta_{t_1t_2}$ are depicted in Fig. 4, the angle sum ω_p is the inwards opening solid angle at vertex p, and the summation is done over edges (p,q), $q \in N_p$.

The sign of the edge angle $\beta_{t_1t_2}$ is determined by a vector blade handedness sign (a determinant sign) of an edge $(p,q) = t_1 \cap t_2$ between triangles $t_1 = (a,p,q)$ and $t_2 = (q,p,b)$, see Eq. 14. Note that the edge sign is positive for pikes (the situation depicted in Fig. 4) and symmetric: $sgn(t_1,t_2) = sgn(t_2,t_1)$. The normals n_t are a result of earlier stages of the computational process.

Also the solid angle ω_p in Eq. 17 is already available from the preceding solid angle filtering (SAF), which can be done to reduce the noise level of the point cloud or for filtering out the foliage signal (Nevalainen et al., 2016), or before any shape classification via curvature spectrum. Availability of spatial angles ω_p makes this method computationally the cheapest one.

In some applications like tumor detection in electron magnetic resonance (EMR) imaging, the orientation of the surface normal n_p is completely free (but outwards from the tumor). That is why the edge signum refers only to two adjoined triangles t_1 and t_2 which are both oriented outwards. The signum in Eq. 15 requires one vector operation (saxpy, see (Golub and Van Loan, 1996)) of $\mathbb{R}^3$ vectors.

Barycentric interpolation (Theisel et al., 2004) is based on normalized linear change of the normal n over the triangle t from where a generic expression for Gaussian and mean curvature can be deduced. For our purposes only the mean curvature H_{tp} of triangle $t = (a,b,c)$ at a vertex point $p \in \{a,b,c\}$ needs to be considered. The Eq. 18 is adapted to our notation from (Theisel et al., 2004; Nevalainen et al., 2015):

$$\begin{aligned} h = &\quad n_a \times (c-b) + n_b \times (a-c) + n_c \times (b-a) \\ H_{tp} = &\quad (n_p \cdot h)/(2n_p \cdot N_t) \qquad (18) \\ H_{tp} \to &\quad H_p, \qquad (19) \end{aligned}$$

where h is a temporary vector multiplicant.

There is also a triangular approximation of the second fundamental form (Crane et al., 2013; Rusinkiewicz, 2004), which is used in (Rusinkiewicz, 2004) to derive the principal curvatures, mean and Gaussian curvature principal and directions directly. This method requires iteration of a least squares problem, and it seems to be computationally more expensive than the methods covered here.

There are other possible interpolation schemes over a triangle, e.g. using radial basis or by applying the well-known Rodriguez rotation formula (Dorst et al., 2007) twice (first over one edge, then between edge and a vertex of interest). Preliminary tests indicate that these options seem to lead to more complex formulas yet the numerical results stay very close to the schemes included to this study. This holds to both the triangular and the vertex values.

2.7 Principal Curvature Orientation

The curvature eigenvalues κ_{t1} and κ_{t2} of a triangle t are the curvature extremals when tracing a continuous surface S through point p by a perpendicular plane:

$$\kappa_{tl} = H_t \pm \sqrt{H_t^2 - G_t}, l = 1,2 \qquad (20)$$

Object and shape recognition may use any subset of the four curvature characteristics G, H, κ_1, κ_2.

The barycentric surface normal map $t \to t^u$ was used to derive Eq. 5. By applying it again, but this time to find a trajectory with most drastic curvature effect per traversed arc length on a triangle t, one gets the principal curvature direction v_t of a triangle t. This is a direction with the largest curvature (eigenvector of κ_1). The second eigenvector is not of interest, since it will be dictated by the first eigenvector. Another

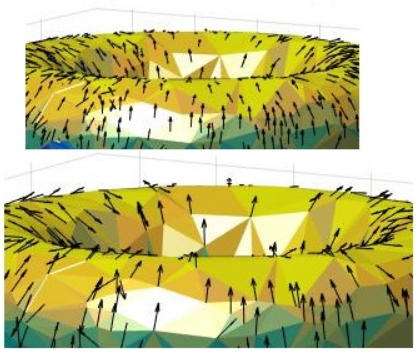

Figure 5: Averaging principal curvature direction v_t from triangles (above) to vertices v_p (below).

way to express v_t is based on constraining the second fundamental form to be diagonal and solving the principal direction from this constraint at Eq. 21. This is different from (Rusinkiewicz, 2004), where whole the second fundamental form is solved by least squares fitting a set of linear constraints. Below are the equations leading to the eigenvalue problem:

$$\begin{aligned} {}'m_a = &\quad P(b-c)(a-c) \text{ (before scaling)} \\ {}'m_b = &\quad P(a-c)(b-c) \text{ (before scaling)} \\ m_a = &\quad \frac{{}'m_a}{{}'m_a \cdot (a-c)} \\ m_b = &\quad \frac{{}'m_b}{{}'m_b \cdot (b-c)} \\ D_t = &\quad (n_a - n_c) m_a^T + (n_b - n_c) m_b^T \\ P(n_t) D_t v_t = &\quad \lambda v_t, \qquad (21) \end{aligned}$$

where ${}'m_a, {}'m_b, m_a' m_b$ are constituents of a constant matrix $D_t = dn_t/dq$, the rate of change of the normal at triangle t. Note that eigenvalue λ is not proportional to principal curvature, since the barymetric mapping does not preserve the unity of the normals.

The weighted summation scheme $v_t \to v_p$ of Eq. 10 is not directly applicable, since the principal directions $\pm v_t$ are defined by the orientation only, without a coherent sign. The summation must take this into account. The following heuristics relies on the monotonic nature of the vector summation of the non-unit cumulative vector $\hat{v}_p$:

$$\begin{aligned} \hat{v}_p(S) = &\quad P(n_p) \textstyle\sum_{t \in T_p} \phi_{tp}' \, sgn_{tp} \, v_t \\ S^* = &\quad \operatorname{argmax}_S \|\hat{v}_p(S)\| \\ v_p = &\quad (\hat{v}_p(S^*))^0, \qquad (22) \end{aligned}$$

where S is the set of signums $S = \{sgn_{tp}\}_{t \in T_p}$, which can be found performing $O(|T_p|)$ scalar products

$\hat{v}_{p\,current} \cdot v_t$ by a single enumeration and reversing a subset of signums if necessary.

The weighting scheme in Eq. 22 relies on the projected tip angle weights ϕ'_{tp}, which have multiple applications and thus can be amortized from computational cost. The weighting scheme in (Rusinkiewicz, 2004) uses triangular contributions of the vertex specific area A'_p. This weighting scheme has not been tested by us. Overall, avoiding the least squares fit and area weighting makes our method less expensive computationally.

3 NUMERICAL EXPERIMENTS

Two synthetical models and a visual inspection of a practical problem have been covered, see Sections 3.1- 3.3. The following mean curvature methods have been compared:

1. triangular average mean curvature (our method)
2. L-B (Meyer et al., 2003)
3. concentrated mean curvature (Mesmoudi et al., 2012)
4. barycentric interpolation of the normal (Theisel et al., 2004)

Two Gaussian curvatures have been compared, triangular average Gaussian (our method, Eq. 4), and vertex Gaussian (Crane et al., 2013). Since there are 3 vertex normal definitions, 2 weighted summation policies, 4 mean curvature and 2 Gaussian curvature definitions, results of only the most interesting combinations have been provided.

3.1 A Local Pike

This model demonstrates the different character of each methods with respect to noise in the surface normal direction. Especially the two noise modes presented in Fig. 1 are modelled. The case 1 in Fig. 6 is an apex of a larger regular formation. The case 2 is a single pike which can be either noise or a useful feature. The case 3 demonstrates a large noise field at the highest possible frequency dictated by point cloud density. The geometrical mean $\sqrt{|G|} = \kappa_G$ derived from the Gaussian curvature G is used for the comparisons, since it has the same physical dimension (inverse of radius) as the mean curvature.

The abscissa value h is the height of point p. When $h \to 0$, it is the planar special case with nominal radius $r \to \infty$ and $\kappa r \to 1$.

The barycentric method exaggerates curvature at large h values, which are likely to be noise. The barycentric mean curvature and the triangular curvatures

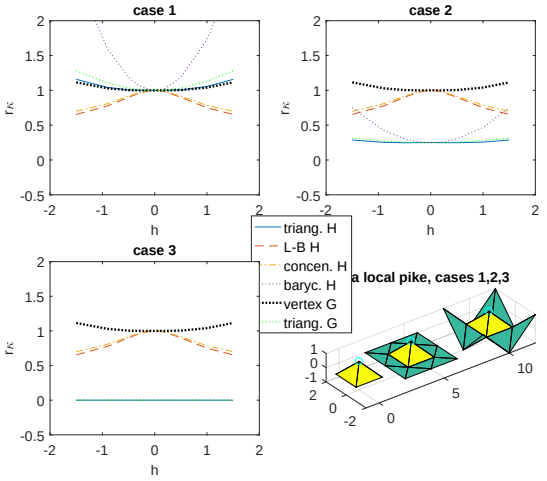

Figure 6: Four mean curvature methods and two Gaussian curvature methods compared in various settings with one point protruding out. The square root of the Gaussian curvature is used for comparison. The analysis point at height h has been circled.

(our methods, both G and H) tend to dampen a singular pike (case 2). The barycentric method is losing its dampening tendency at high values of h, which are more likely to be noise.

The output value of the vertex mean and Gaussian curvatures (and barycentric mean curvature) is scaled downwards (dampened) by a ratio w, value of which depends on the case. The cases $1,2,3$ have dampening ratios $w = 1, 1/3, 0$. A singular pike (case 2) has dampening factor $1/3$ which is still adequate to contribute in the curvature spectrum or to be detected by later pattern recognition phase.

The egg cell pattern of case 3 gets completely dampened by triangular curvatures G and H, and by the barycentric method. The vertex normals defined by Eqs. 2 and 10 become parallel, which then causes the triangular curvatures of the involved triangles t to be zero, see Eqs. 5 and 4. This can be a useful property in some applications, e.g. in stone detection (Nevalainen et al., 2016), or in reducing the granularity effect produced by voxels.

The concentrated curvature, vertex Gaussian, and Laplace-Beltrami are closely related in all cases. The behaviour of all six methods is rather similar to each other in the hyperbolical case (a saddle point) and this case has not been included in this presentation.

3.2 A Torus

A torus of radii $r = 1, R = 2.5$ has been used. This is a classical test case, since the curvature aspects of the ideal shape are analytical, yet both elliptic and hyper-

bolic local surface metrics occurs.

Two torii, a dense one with $|\mathcal{P}| = 820$ and a sparse one with $|\mathcal{P}| = 220$ were used. Fig. 7 shows the sparse torus with uniform local height distribution. A uniform distribution is used also on the tangential manifold metrics. The height noise concerns point locations and the tangential noise concerns triangulation irregularity. The height noise std. was varied between $0 \leq \sigma_h \leq 0.3r$. The upper end of the noise is typical to many LiDAR applications. The height noise distributions from real LiDAR data are not uniform nor Gaussian. The main curvature spectrum seems to depend mainly on the std of the uniform or natural height distribution, not from the choice between the two.

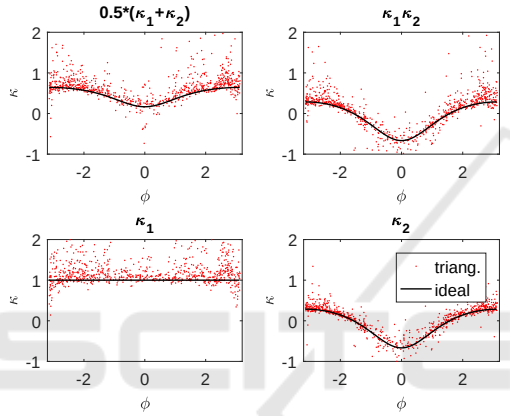

Figure 7: The triangular mean curvature and triangular Gaussian curvature and two curvature eigenvalues on a torus as a function of the angle ϕ associated with the smaller radius. The height noise is at the maximum $\sigma_h/r = 0.3$.

3.3 A Prostate Tumor

The main difficulty with MRI point clouds arises from the anisotropy of the point cloud. The voxels are elongated $2.75 \times 0.48 \times 0.48\ mm^3$ and this demands a lot from the curvature analysis methods. Information about the curvature spectrum of the tumor has been applied to e.g. breast cancer classification (Lee et al., 2015). It is possible that the curvature spectrum will be an important feature alongside spatial texture patterns, 3D Fourier transform, overall size and location of the tumor for clustering algorithms. The Gaussian curvature and principal curvature direction can help in e.g. descriptor based vectorization (Vranic and Saupe, 2001). Fig. 10 depicts a prostate lesion, which shows a typical developable shape: the lesion could be spread back to planar (its Gaussian curvature is approximately zero).

3.4 Results

Our method, when referred, means triangular mean and Gaussian (Eqs. 5, 4, 10) and the principal curvatures derived from them. Tests reach the high noise amplitude range $\sigma_h/r = 0.3$ typical to the natural resource data, see Fig. 7. Effects of noise filtering of L-B and our method have been depicted in Fig. 8. L-B is bound by its fidelity to local geometry. Difference at smooth surface (the left part of the abscissa) is due to the irregularity of the triangles, which brings some advantage to an averaging method like ours.

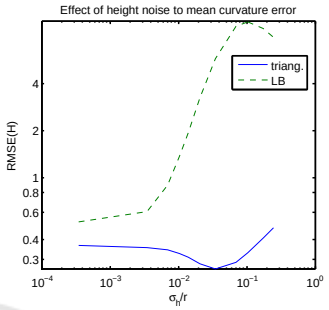

Figure 8: The root mean square error of the mean curvature H estimation error under different perpendicular noise levels σ_h (std.) on a torus with radii r and R.

Fig. 9 has curvature spectrae based on L-B and our method. Other methods were inferior at the noisy end and had to be excluded. The presence of noise spreads the detected spectrum from the ideal smooth case. L-B manages the task only if the triangularization is rather regular and the height noise almost zero. Our method captures two-thirds of the mean curvature distribution, yet suffers from the spectrum spread caused by the noise, which is inevitable. Both Gaussian approximations perform as well enabling e.g. the curvature spectrum classification to be possible under wide range of noise levels. Other two methods (concentrated and barycentric) perform worse than L-B.

Fig. 10 depicts the prostate lesion with the Gaussian curvature close to zero everywhere meaning its surface is mostly developable (a so called ruler surface). This is an artifact caused by a combination of the elongated voxels and the method used for triangularization. The surface has high energy noise component caused by the voxel granularity. Our methods dampen this highest geometric noise component automatically. Also concentrated and barycentric mean curvatures performs surprisingly well. L-B suffers from its fidelity to the highest shape frequency component.

The computational cost of the barycentric method is too high when compared to its performance, see

Table 1: Evaluation of the mean curvature methods. Proposed methods in boldface.

Method	Vector opers/t	Spectrum quality	Singular noise w	Massive noise w
vertex G	15	good	1	1
triangular G	15	good	1/3	0
triangular H	15	good	1/3	0
LB	18	average	1	1
concentrated	2	poor	1	1
barycentric	32	poor	1/3	0

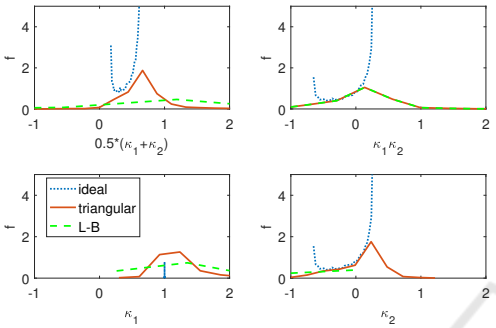

Figure 9: The ideal curvature spectra of a torus with $r = 1$, and Laplace-Beltrami and triangular approximations. The effect of height noise $\sigma_h/r = 0.1$ spreads out the approximated spectrae.

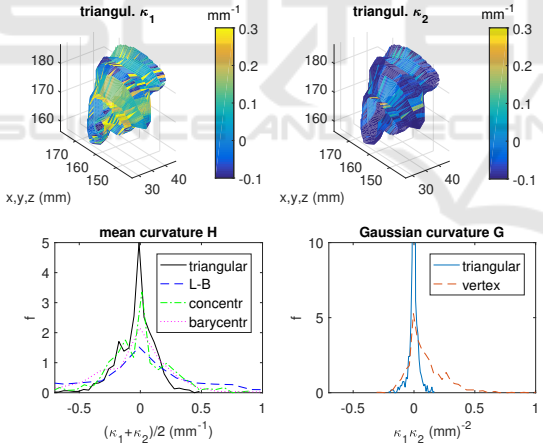

Figure 10: Upper row: the principal curvature components. Lower row: Distributions of the mean and Gaussian curvatures by different methods.

Table 1. L-B has the best accuracy when the perpendicular noise is small and the triangulation is rather regular, but fails when the perpendicular noise is high. The spectrum quality is given a qualitative judgement. See the definition of the dampening ratio w at Sec. 3.1.

4 CONCLUSIONS

The proposed method (triangular mean and Gaussian curvature) has about the same computational demand as the reference method (LB mean and vertex Gaussian curvature) in case where the vertex specific area A'_p of the mixed Voronoi cell is computed exactly as recommended in (Mesmoudi et al., 2012). Based on the good performance under height noise, it seems that the triangular method should be used in such natural resource data applications, where the curvature spectrum is required, and the spectral range should reach near the highest shape frequency, but excluding the large excitations of the mentioned frequency.

The above definition may seem contrived, but e.g. a typical rasterization process is lossy and tuning the filtering process requires a lot of parameters, which concern the highest shape frequency naturally contained with the methods proposed here. Further validation is necessary with e.g. track analysis of forestry harvesters (Pierzchala et al., 2016).

Principal orientation computation presented in Sec. 2.7 is closely related to other two methods presented, e.g. it uses the same projected tip angle weights. One has to inspect in the future how useful the principal orientations are in micro-topographic analysis. It may be that a multi-scale approach for producing several TIN models with coherent curvature and principal orientation information is needed.

There is a huge bulk of raster analysis methods and a lot of experience in applying these methods for e.g. height raster data analysis. Emerging triangular analysis tools based on DDG will not outdate these methods, but in some cases there seems to be potential to improve the curvature spectrum range closer to the theoretical limit dictated by the point cloud sample density and the known sample accuracy.

ACKNOWLEDGEMENTS

This work was supported by the funding from the Academy of Finland (Grant 295336). Kevin R. Vixie

and Otis Chodosh brought up the intuitive view to mean curvature on Math Overflow site on 2012.

REFERENCES

Crane, K., de Goes, F., Desbrun, M., and Schröder, P. (2013). Digital geometry processing with discrete exterior calculus. In *ACM SIGGRAPH 2013 Courses*, SIGGRAPH '13, pages 7:1–7:126, New York, NY, USA. ACM.

Dorst, L., Fontijne, D., and Mann, S. (2007). *Geometric Algebra for Computer Science: An Object-Oriented Approach to Geometry*. Morgan Kaufmann Publishers Inc., San Francisco, CA, USA, 1st edition.

Golub, G. H. and Van Loan, C. F. (1996). *Matrix Computations (3rd Ed.)*. Johns Hopkins University Press, Baltimore, MD, USA.

Jin, S., Lewis, R., and West, D. (2005). A comparison of algorithms for vertex normal computation. *The Visual Computer*, 21:71–82.

Lee, J., Nishikawa, R. M., Reiser, I., Boone, J. M., and Lindfors, K. K. (2015). Local curvature analysis for classifying breast tumors: Preliminary analysis in dedicated breast ct. *Medical Physics*, 42(9).

Max, N. (1999). Weights for computing vertex normals from facet normals. *Journal of Graphics Tools*, 4(2).

Mesmoudi, M. M., De Floriani, L., and Magillo, P. (2012). Discrete curvature estimation methods for triangulated surfaces. In *Applications of Discrete Geometry and Mathematical Morphology*, pages 28–42. Springer.

Meyer, M., Desbrun, M., Schröder, P., and Barr, A. H. (2003). *Visualization and Mathematics III*, chapter Discrete Differential-Geometry Operators for Triangulated 2-Manifolds, pages 35–57. Springer Berlin Heidelberg, Berlin, Heidelberg.

Mitra, N. J. and Nguyen, A. (2003). Estimating surface normals in noisy point cloud data. In *Proceedings of the Nineteenth Annual Symposium on Computational Geometry*, SCG03, pages 322–328, New York, NY, USA. ACM.

Nevalainen, P., Middleton, M., Kaate, I., Pahikkala, T., Sutinen, R., and Heikkonen, J. (2015). Detecting stony areas based on ground surface curvature distribution. In *2015 International Conference on Image Processing Theory, Tools and Applications, IPTA 2015, Orleans, France, November 10-13, 2015*, pages 581–587.

Nevalainen, P., Middleton, M., Sutinen, R., Heikkonen, J., and Pahikkala, T. (2016). Detecting terrain stoniness from airborne laser scanning data . *Remote Sensing*, 8(9):720.

Pierzchala, M., Talbot, B., and Astrup, R. (2016). Measuring wheel ruts with close-range photogrammetry. *Forestry*, 89(4):383–391.

Pressley, A. (2010). *Elementary Differential Geometry*. Springer Undergraduate Mathematics Series. Springer London.

Rusinkiewicz, S. (2004). Estimating curvatures and their derivatives on triangle meshes. In *Symposium on 3D Data Processing, Visualization, and Transmission*.

Schaer, P., Skaloud, J., Landtwing, S., and Legat, K. (2007). Accuracy Estimation for Laser Point Cloud Including Scanning Geometry. In *Mobile Mapping Symposium 2007, Padova*.

Theisel, H., Rössl, C., Zayer, R., and Seidel, H. P. (2004). Normal based estimation of the curvature tensor for triangular meshes. In *In PG04: Proceedings of the Computer Graphics and Applications, 12th Pacific Conference on (PG2004)*, pages 288–297. IEEE Computer Society.

van Oosterom, A. and Strackee, J. (1983). A solid angle of a plane triangle. *IEEE Trans. Biomed. Eng.*, 30(2):125–126.

Vranic, D. V. and Saupe, D. (2001). 3d shape descriptor based on 3d fourier transform. In Fazekas, K., editor, *3D Shape Descriptor Based on 3D Fourier Transform In Proceedings of the EURASIP Conference on Digital Signal Processing for Multimedia Communications and Services (ECMCS 2001)*, pages 271–274.

Wardetzky, M., Mathur, S., Kaelberer, F., and Grinspun, E. (2007). Discrete laplace operators: No free lunch. In Belyaev, A. and Garland, M., editors, *Geometry Processing*. The Eurographics Association.

Yang, P. and Qian, X. (2007). Direct computing of surface curvatures for point-set surfaces. In *SPBG'07*, pages 29–36.